

## Kirigami-Inspired Thermal Regulator

Hongyi Ouyang,<sup>1,§</sup> Yuanqing Gu,<sup>2,3,§</sup> Zhibin Gao<sup>1,\*,</sup> Lei Hu,<sup>1</sup> Zhen Zhang,<sup>1</sup> Jie Ren<sup>1,4</sup>, Baowen Li,<sup>5,6,7</sup> Jun Sun,<sup>1</sup> Yan Chen,<sup>2,3,†</sup> and Xiangdong Ding<sup>1,‡</sup>

<sup>1</sup>State Key Laboratory for Mechanical Behavior of Materials, Xi'an Jiaotong University, Xi'an 710049, China

<sup>2</sup>Key Laboratory of Mechanism and Equipment Design of Ministry of Education, Tianjin University, Tianjin 300350, China

<sup>3</sup>School of Mechanical Engineering, Tianjin University, Tianjin 300350, China

<sup>4</sup>Center for Phononics and Thermal Energy Science, China-EU Joint Center for Nanophononics, Shanghai Key Laboratory of Special Artificial Microstructure Materials and Technology, School of Physics Sciences and Engineering, Tongji University, Shanghai 200092, China

<sup>5</sup>Department of Materials Science and Engineering, Department of Physics, Southern University of Science and Technology, Shenzhen 518055, People's Republic of China

<sup>6</sup>International Quantum Academy, Shenzhen 518048, People's Republic of China

<sup>7</sup>Paul M. Rady Department of Mechanical Engineering and Department of Physics, University of Colorado, Boulder, Colorado 80305-0427, USA



(Received 8 September 2022; revised 7 December 2022; accepted 16 December 2022; published 13 January 2023)

One of the current challenges in nanoscience is tailoring phononic devices, such as thermal regulators and thermal computing. This has long been a rather elusive task because the thermal-switching ratio is not as high as electronic analogs. Mapping from a topological kirigami assembly, nitrogen-doped porous graphene metamaterials on the nanoscale are inversely designed with a thermal-switching ratio of 27.79, which is more than double the value of previous work. We trace this behavior to the chiral folding-unfolding deformation, resulting in a metal-insulator transition. This study provides a nanomaterial design paradigm to bridge the gap between kinematics and functional metamaterials that motivates the development of high-performance thermal regulators.

DOI: 10.1103/PhysRevApplied.19.L011001

Thermal regulation is the most critical technology challenge for modern electronics [1,2], thermoelectricity [3], thermal cooling [4,5], interfacial thermal resistance [6], and phononics [7,8]. Similar to electrical switches, thermal regulators whose thermal transport in two states or directions is relatively different from each other [9–11] and play roles in thermal storage, thermal management, and solid-state thermal circuits [12–15]. To regulate the thermal conductivity  $\kappa$ , researchers focused on the modulation between two states and mechanisms that facilitate large thermal-switching ratio  $R$  between on-state high thermal conductivity  $\kappa_{\text{on}}$  and off-state low thermal conductivity  $\kappa_{\text{off}}$ .

Several materials have been unveiled with thermal-switching behavior under different kinds of incentives [16], such as shape memory alloy [17,18], shape-dependent nanoislands [19], monolayer lateral heterojunction [20],

multibody effect in radiation [21], strain in ferroelectric domain [22] and in compressible graphene [23], thermophile proteins [24], plasmon resonators [25], local effect in polymer [26], electric field [27,28], magnetic field [29], temperature-induced phase transition [30], temperature-dependent transformation thermotics, element substitution [31], electrochemical reaction [32,33], optical excitation [34], and even hydration in bioinspired materials [35]. Although these studies have reported up to an order of magnitude in switching ratios and corresponding mechanisms, how to further augment  $R$  for high-performance thermal regulators is still a conundrum and limits their applications.

In this Letter, we design a two-dimensional (2D) honeycomb kirigami assembly using metamaterial and map it on porous graphene. Chirality is induced by nitrogen substitution, realizing asymmetrical folding-unfolding deformation. We find nitrogen-doped porous graphene (NPG) can exhibit an ultrahigh  $R$  of 27.78 under only 1% strain. With this small deformation, the obvious change is found in the band structure, resulting in an unusual metal-insulator transition and enhanced optical absorption in NPG. Our work offers a nanomaterial design paradigm mapping from

\*zhibin.gao@xjtu.edu.cn

†yan\_chen@tju.edu.cn

‡dingxd@mail.xjtu.edu.cn

§These authors contributed equally to this work.

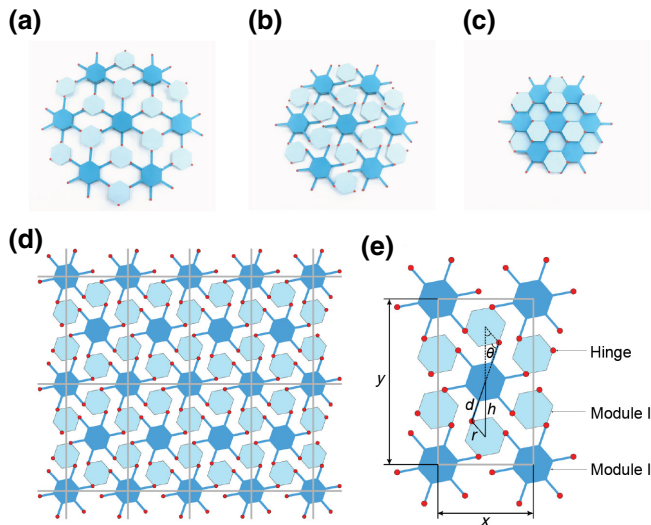


FIG. 1. Kirigami assembly consisting of regular hexagons. (a)–(c) Snapshots of the physical prototype in unfolding, intermediate, and fully closed states, respectively. Hinge points are shown by red dots. (d) Periodic tessellation is displayed by gray rectangles. (e) Geometric parameters are defined in the unit cell.

topological assembly on metamaterials, showing potential high-performance thermal regulators.

The 2D honeycomb kirigami assembly based on the nanoporous graphene with the folding-unfolding deformation, shown in Fig. 1. It consists of two modules, one of which is module I having a hexagon with three hinge points (light blue). Another one is module II, a similar hexagon with six arms (dark blue). The endpoints of the arms are connected with module I by hinges. The kirigami model enables the entire assembly with one degree-of-freedom motion and avoids physical interference. Snapshots of kirigami assembly during deformation are shown in Figs. 1(a)–1(c), and the tessellation is presented in Fig. 1(d). The folding-unfolding deformation for the kirigami assembly is depicted in Video S1 within the Supplemental Material [36].

Geometric parameters of the kirigami assembly are illustrated in Fig. 1(e).  $r$  and  $d$  are the distance between center modules and hinge points in modules I and II, respectively.  $h$  is the distance between the center of two modules and  $\theta$  is the angle between module I and the adjacent arm. A periodical rectangular unit cell is depicted in the kirigami assembly, which is more easily to determine the strain in the Cartesian coordinate system. Then we investigate the deformation behavior of the assembly,

$$h = \sqrt{d^2 + r^2 - 2dr \cdot \cos(\theta + \pi/3)}, \quad (1)$$

$$x = \sqrt{3}h, \quad y = 3h. \quad (2)$$

In the following, we map the kirigami assembly on 2D mechanical metamaterials. The point-to-point rigid rod

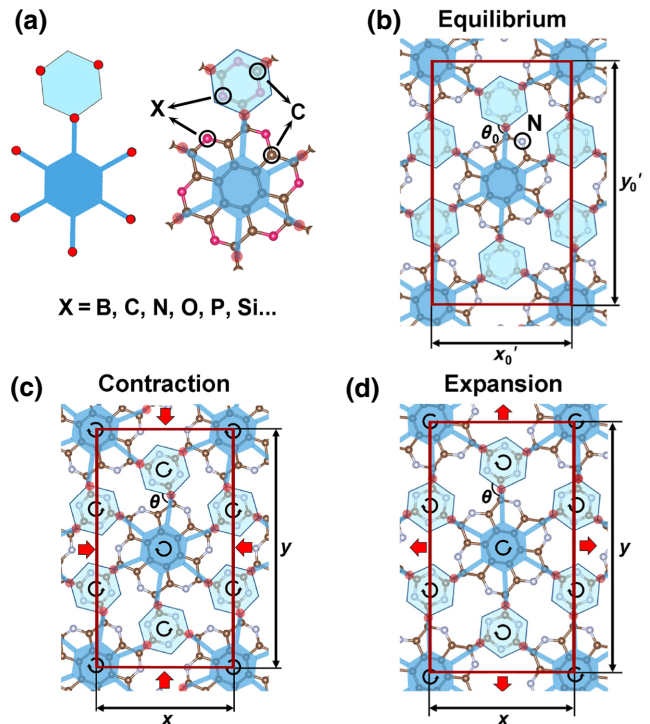


FIG. 2. Mapping of kirigami assembly to metamaterials. (a) Module I and II are replaced by one honeycomb and a cluster including seven honeycombs. The element of pink atoms labeled by  $X$  is to be decided shown within the Supplemental Material [36]. Snapshots of NPG in (b) equilibrium, (c) contraction, and (d) expansion states during deformation. Black arrows indicate the rotation of modules. The brown and white balls are C and N, respectively.

connections in kirigami assembly are replaced by chemical bonds. According to the spatial linkage kinematics about the relationship between cyclohexane molecular and octahedral Bricard 6R linkage [37], we call the bond connecting different modules as “hinge bond” and treat the midpoints of the “hinge bond” as hinges. Therefore, two components are designed to represent two modules in the assembly, as shown in Fig. 2(a). To increase the stability of the structure, carbocyclic six-membered rings are kept. What is more, chirality can be induced by elemental substitution, resulting in the asymmetrical folding-unfolding deformation in metamaterials.

Since the potential element is selected, we set criteria to guide the element selection labeled  $X$  shown in Fig. 2(a), which include (i) obvious distortion out of plane should be avoided that will preclude the deformation, (ii) the connection between two types of modules should be only one chemical bond to ensure the flexibility of the whole structure, (iii) the electronic band structure in the equilibrium state should be an insulator to realize the metal-insulator transition by small deformation. The whole detail of the selection process with element  $X$  is discussed within the

Supplemental Material [36,49]. Consequently, the nitrogen element is the best one of X and we focus on the nitrogen porous graphene, named NPG.

We acquire the optimized metamaterials with different lattice constants and  $\theta$  by density-functional theory (DFT). The details of calculation are shown within the Supplemental Material [36,50–55]. Interestingly, NPG in Figs. 2(b)–2(d) and Video S2 within the Supplemental Material [36] performs a similar folding-unfolding deformation behavior after contraction or expansion, corresponding to the kirigami assembly in Figs. 1(a)–1(c). The most stable structure has a  $\theta_0$  of  $110.73^\circ$ , which is slightly different from the assembly with  $120^\circ$ .

We unexpectedly find that NPG has a property of chirality, which means the rotation in clockwise and anti-clockwise exhibit different deformation behaviors [56]. The more mechanical property of NPG is discussed within the Supplemental Material [36].

Now we address the crucial issue, namely, deformation effect on the electronic and thermal properties. Thermal conductivity can be divided into two parts. Based on *ab initio* and nonequilibrium molecular dynamics simulation, we can obtain  $\kappa_{\text{lat}}$  and  $\kappa_{\text{el}}$  by Fourier law and Wiedemann-Franz (WF) law,

$$\kappa_{\text{lat}} = -\frac{J}{\nabla T}, \quad \kappa_{\text{el}} = L_0 \sigma T, \quad (3)$$

where  $J$  is the heat flux of energy transport per unit time across the unit area that is defined as  $S = W \times d$  in which  $W$  is the width of the 2D sheet and  $d$  is the interlayer distance for the corresponding bulk material ( $d = 3.355 \text{ \AA}$  for NPG).  $\nabla T$  is the temperature gradient along the heat-transport direction.  $\sigma$  is the electric conductivity and  $L_0$  is the Lorenz constant number of  $2.44 \times 10^{-8} \text{ W } \Omega \text{ K}^{-2}$ .

The discussion about why WF law is suited to NPG [57–62], details of calculation [63,64], and length dependence of  $\kappa_{\text{lat}}$  [65–68] are shown within the Supplemental Material [36].

We find that the change of  $\kappa_{\text{lat}}$  is not obvious as a function of strain, while  $\kappa_{\text{el}}$  increases by 7 orders of magnitude after contraction of only 1% strain shown in Fig. 3(a). This discovery will result in a dominating role of  $\kappa_{\text{el}}$  compared with  $\kappa_{\text{lat}}$ .  $\kappa_{\text{lat}}$  has a value of  $8.92 \text{ W/mK}$  in equilibrium state and fluctuates slightly to  $9.05 \text{ W/mK}$  with 1% compressive strain.  $\kappa_{\text{el}}$  of different doping carriers and concentrations are shown in Fig. S12 within the Supplemental Material [36].

Thermal-switching ratio  $R$  is the key parameter to evaluate ability of the thermal switch,  $R = \kappa_{\text{on}}/\kappa_{\text{off}}$ , where  $\kappa_{\text{on}}$  is the largest  $\kappa$  in the “on” state, and  $\kappa_{\text{off}}$  is the smallest  $\kappa$  in the “off” state. Let us now attempt the relationship between  $R$  and strain at four different typical doping concentrations. For instance, at  $5 \times 10^{-14} \text{ cm}^{-2}$  hole-doping concentration,  $\kappa_{\text{el}}$  is equal to  $8.97 \times 10^{-6} \text{ W/mK}$  in the equilibrium state, while  $238.87 \text{ W/mK}$  with only 1% compressive strain. The total thermal conductivity changes from  $8.92 \text{ W/mK}$  without strain to  $247.92 \text{ W/mK}$  with 1% compressive strain, achieving  $R = 27.79$ , shown in Fig. 3(b). Furthermore,  $R$  in compressive strain is much larger than that of tensile strain, indicating an obvious chirality of NPG. At a given strain,  $R$  is directly proportional to the doping concentration, and the relative discrepancy of  $R$  between different doping levels increases as a function of strain.

Referring to most of the former research about thermal management materials such as  $\text{VO}_2$ , PE nanofiber, and other phase-change materials [30,34,40–48]. We collect  $R$  of all these interesting works combined with our NPG

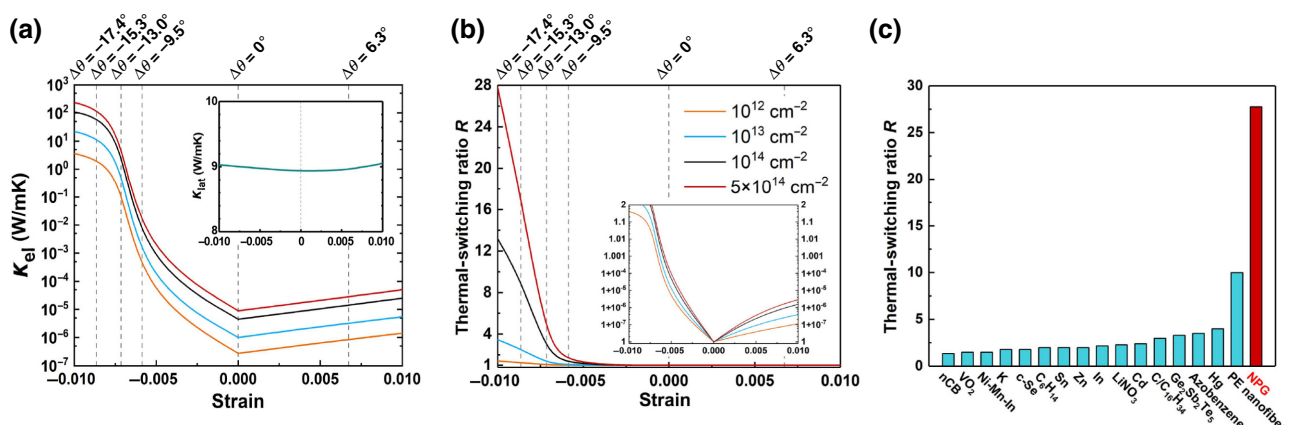


FIG. 3. (a)  $\kappa_{\text{el}}$  and  $\kappa_{\text{lat}}$  (inset) of NPG as functions of strain. (b) Thermal-switching ratio  $R$  versus strain under different hole-carrier concentrations. The enlarged feature of  $R$  between 1 and 2 is shown in the inset. A maximum doping level of  $5 \times 10^{-14} \text{ cm}^{-2}$  for both electrons and holes is reached by electrical gating [38] and ionic liquid injection [39]. (c)  $R$  of NPG compared with reported thermal regulators. nCB [40]; VO<sub>2</sub> [41]; K, Zn, Cd, and Hg [42]; c-Se [43]; Ni-Mn-In alloy [44]; C<sub>6</sub>H<sub>14</sub> [45]; Sn, In, and LiNO<sub>3</sub> [46]; C/C<sub>16</sub>H<sub>34</sub> composite [47]; Ge<sub>2</sub>Sb<sub>2</sub>Te<sub>5</sub> [48]; azobenzene polymers [34]; PE nanofiber [30].

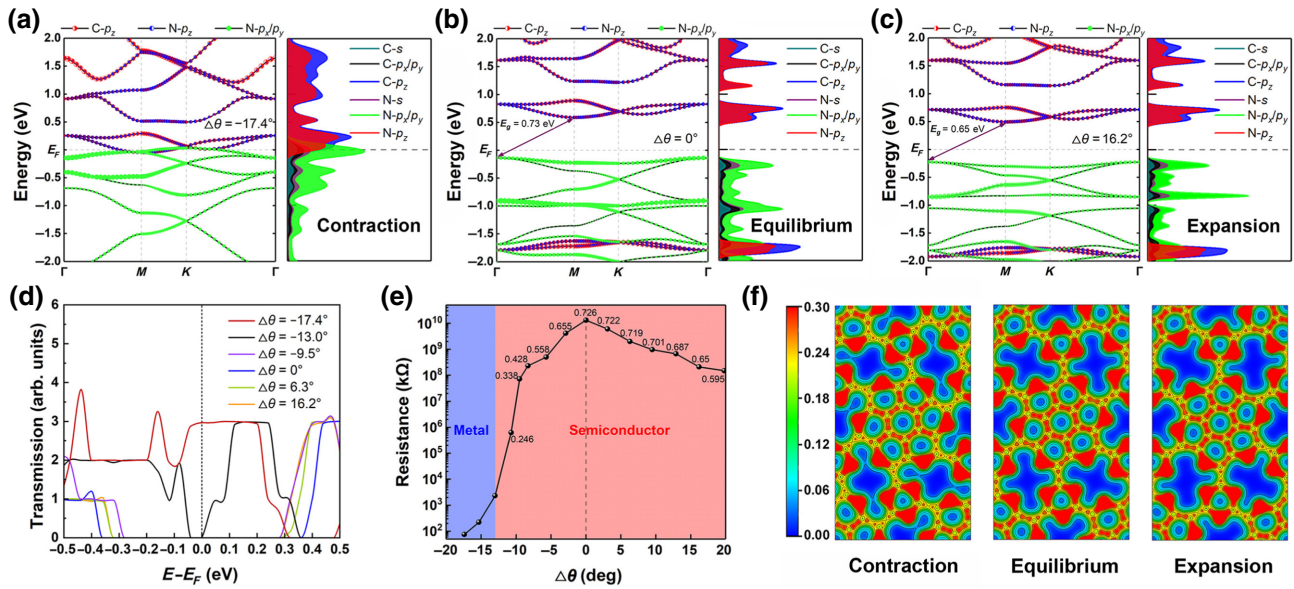


FIG. 4. (a)–(c) Projected band structures and PDOS of NPG in three deformation states. (d) Electronic transmission spectrum and (e) electrical resistance of the NPG device with different  $\Delta\theta$ . Fermi level is regarded to be zero for each state to compare the transfer ability of electrons between electrodes among all states. The number in (e) stands for the band gap  $E_g$  in the eV unit. (f) The isosurface plot of the charge density of NPG and the isosurface value is taken as  $0.06 \text{ e/Bohr}^3$ .

value, shown in Fig. 3(c), indicating the potential of NPG for manufacturing high-performance thermal regulators.

Remember that the mild change of  $\kappa_{\text{lat}}$  can be originated from the unchanged space group of NPG with  $P6/m$  (175) during deformation, similar to  $\text{VO}_2$  near the phase transition [69]. The physical reason for a wild change of  $\kappa_{\text{el}}$  is the metal-insulator transition, since band structures and projected density of states (PDOS) change significantly shown in Figs. 4(a)–4(c).

With deformation, conduction bands of NPG move downward while valence bands move upward, resulting in a smaller band gap compared with the equilibrium state with  $E_g = 0.73 \text{ eV}$ . Under 1% compression, the band gap closes due to the decrease of distance between atoms, resulting in a shift of the electronic energy states. The projected band structure shows that the conduction-band minimum is dominated by  $p_z$  orbitals of carbon and nitrogen atoms, while the valence-band maximum is controlled by  $p_x$  and  $p_y$  orbitals of nitrogen atoms. Moreover, the band gap of NPG decreases slowly in expansion while declining rapidly in contraction. This phenomenon could be attributed to the chirality of NPG. We also find the main discrepancy of PDOS between the contraction state and the other two states is whether the overlap of  $p_x$ ,  $p_y$ , and  $p_z$  of nitrogen atoms exists, indicating the hybridization of orbits and delocalization of electrons.

The band gap will fall to zero when  $\Delta\theta$  reaches the critical angle of  $-13.0^\circ$ , indicating a metal-insulator transition occurs during deformation. The most adopted method to trigger it, in previous reports, is applying a large 10%

mechanical deformation to adjust the distance between atoms and to redistribute electronic wave function, called Mott transition [70–73]. For NPG, the metal-insulator transition emerges after only 1% change of the lattice constant, which is much easier to be realized by substrate engineering, and could be used as supersensitive pressure sensors in nanomaterials science.

To explore electronic transport properties, we built NPG devices shown in Fig. S13 within the Supplemental Material [36]. Without bias potential, transmission spectrums of different states are shown in Fig. 4(d). Around the Fermi level, there is no transmission for all of them except the state of  $\Delta\theta = -13.0^\circ$  and  $\Delta\theta = -17.4^\circ$ , corresponding semimetal and metal states, respectively. Then electrical resistances of different states are invested by setting the bias voltage range from 0 to 1.0 V, shown in Fig. 4(e). There are 7 orders of magnitude difference in electrical resistance between the state of  $\Delta\theta = -17.4^\circ$  and the equilibrium state, while only 2 orders of magnitude difference between the state of  $\Delta\theta = 16.2^\circ$  and the equilibrium state. The details of calculation are shown within the Supplemental Material [36,74–76].

Let us now attempt the mechanism of the metal-insulator transition at the electronic distribution level. Figure 4(f) presents the charge-density isosurface of NPG in three states. Contraction is more effective than an expansion to decrease the distance between adjacent nitrogen atoms, resulting in delocalizing the state and narrowing the band gap. This microscopic electronic behavior further supports the explanation of the metal-insulator transition in

NPG. Except for the thermal and electrical properties, we also study the optical property and negative thermal expansion [77,78] of NPG shown in Figs. S16 and S17 within the Supplemental Material [36]. Furthermore, we validate the effective medium concept of NPG [79] and discuss the potential methods to obtain NPG [80–88].

Before closing, we briefly discuss the energy cost to obtain such a thermal regulation. The strain energy of NPG is presented in Fig. S18 within the Supplemental Material [36], and by changing the angle  $\theta$  with the  $\pm 15^\circ$  from the equilibrium state, the largest energy needed is 140 meV/atom, about 3% of the carbon bond-breaking energy [89]. Thus, hexagonal rings in NPG are dynamically stable. In *ab initio* molecular-dynamics calculation with two unit cells, the wrinkle along the  $z$  axis is less than 0.05 nm in 300 K. For an extensive area of NPG, the vibration along the  $z$  axis should be close to pure graphene, approximately equal to 1 nm [90], indicating the way of manipulating NPG is like graphene. For instance, the strain is 0.0109 from the equilibrium state ( $\theta = 110.72^\circ$ ) to the expansion state ( $\theta = 120.27^\circ$ ), and the corresponding energy cost per unit cell is 3.114 eV (the area of the unit cell is  $2.2458 \text{ nm}^2$ ). The energy needed is  $0.222 \text{ J m}^{-2}$ , even smaller than the cleavage energy of graphite with a value of  $0.33 \text{ J m}^{-2}$  [89], suggesting that NPG can be manipulated by a relatively small force.

In summary, we exhibit the demonstration of mapping from kirigami assembly on NPG metamaterials at atomic scale whose thermal-switching ratio reaches 27.79 under only 1% strain, which is more than double the value of previous work. It can be stemmed from a metal-insulator transition, which switches the main heat carrier in NPG during the asymmetrical folding-unfolding deformation.

We hope the present results for inversely designing kirigami-inspired thermal switches do invigorate the studies aimed at uncovering intriguing high-performance thermal regulators, thermal diode, and thermal transistor, in the discipline of phononics, which will play essential roles in nanoscale calorimeters and thermal management of microelectronics.

*Acknowledgments.*—We acknowledge the support from the National Natural Science Foundation of China (Grants No. 12104356, No. 52071258, No. 52035008, No. 51825503, No. 52250191) and the Tencent Foundation (XPLORE-2020-1035). Z.G. acknowledges the support of China Postdoctoral Science Foundation (Grant No. 2022M712552) and the Fundamental Research Funds for the Central Universities. We also acknowledge the support by HPC Platform, Xi'an Jiaotong University.

- 
- [1] M. M. Waldrop, *Nature* **530**, 144 (2016).
  - [2] P. Ball, *Nature* **492**, 174 (2012).

- [3] L.-D. Zhao, *et al.*, *Nature* **508**, 373 (2014).
- [4] M. Jiang, *et al.*, *Nature* **601**, 568 (2022).
- [5] L. Lindsay, *et al.*, *Phys. Rev. Lett.* **111**, 025901 (2013).
- [6] J. Chen, *et al.*, *Rev. Mod. Phys.* **94**, 025002 (2022).
- [7] N. Li, *et al.*, *Rev. Mod. Phys.* **84**, 1045 (2012).
- [8] X. Gu, *et al.*, *Rev. Mod. Phys.* **90**, 041002 (2018).
- [9] B. Li, *et al.*, *Phys. Rev. Lett.* **93**, 184301 (2004).
- [10] L. Wang and B. Li, *Phys. Rev. Lett.* **99**, 177208 (2007).
- [11] C. W. Chang, *et al.*, *Science* **314**, 1121 (2006).
- [12] M. J. Martínez-Pérez, *et al.*, *Nat. Nanotechnol.* **10**, 303 (2015).
- [13] L. Wang and B. Li, *Phys. Rev. Lett.* **101**, 267203 (2008).
- [14] G. Wehmeyer, *et al.*, *Appl. Phys. Rev.* **4**, 041304 (2017).
- [15] Y. Li, *et al.*, *Nat. Rev. Mater.* **6**, 488 (2021).
- [16] N. Jiménez, *et al.*, Acoustic waves in periodic structures, metamaterials, and porous media, Ch. the Transfer Matrix Method in Acoustics, Springer International Publishing, Cham, 103 (2021).
- [17] M. Hao, *et al.*, *Nat. Energy* **3**, 899 (2018).
- [18] Y. Li, *et al.*, *Phys. Rev. Lett.* **115**, 195503 (2015).
- [19] M. Bode, *et al.*, *Phys. Rev. Lett.* **92**, 067201 (2004).
- [20] Y. Zhang, *et al.*, *Science* **378**, 169 (2022).
- [21] D. Thompson, *et al.*, *Nat. Nanotechnol.* **15**, 99 (2020).
- [22] E. Langenberg, *et al.*, *Nano Lett.* **19**, 7901 (2019).
- [23] T. Du, *et al.*, *Nat. Commun.* **12**, 1 (2021).
- [24] T. Nonoyama, *et al.*, *Adv. Mater.* **32**, 1905878 (2020).
- [25] O. Ilic, *et al.*, *ACS Nano* **12**, 2474 (2018).
- [26] D. Azulay, *et al.*, *Phys. Rev. Lett.* **90**, 236601 (2003).
- [27] J. F. Ihlefeld, *et al.*, *Nano Lett.* **15**, 1791 (2015).
- [28] C. Liu, *et al.*, *Phys. Rev. Appl.* **11**, 044002 (2019).
- [29] J. Shin, *et al.*, *ACS Macro Lett.* **5**, 955 (2016).
- [30] R. Shrestha, *et al.*, *Sci. Adv.* **5**, eaax3777 (2019).
- [31] K. Aryana, *et al.*, *Nat. Commun.* **12**, 1 (2021).
- [32] J. Cho, *et al.*, *Nat. Commun.* **5**, 1 (2014).
- [33] Q. Lu, *et al.*, *Nat. Mater.* **19**, 655 (2020).
- [34] J. Shin, *et al.*, *Proc. Natl Acad. Sci. USA* **116**, 5973 (2019).
- [35] J. A. Tomko, *et al.*, *Nat. Nanotechnol.* **13**, 959 (2018).
- [36] See Supplemental Material at <http://link.aps.org-supplemental/10.1103/PhysRevApplied.19.L011001>. Details of calculation, element X selecting process, stability, mechanical properties, thermal/electronic transport properties, and optical properties of NPG are discussed in Supplemental Material. The folding-unfolding deformation for the kirigami assembly and NPG is depicted in Video S1 and Video S2.
- [37] J. E. Baker, *Mech. Mach. Theory* **21**, 253 (1986).
- [38] D. K. Efetov and P. Kim, *Phys. Rev. Lett.* **105**, 256805 (2010).
- [39] H.-J. Chuang, *et al.*, *Nano Lett.* **14**, 3594 (2014).
- [40] M. Marinelli, *et al.*, *Phys. Rev. E* **58**, 5860 (1998).
- [41] D.-W. Oh, *et al.*, *Appl. Phys. Lett.* **96**, 151906 (2010).
- [42] C. Y. Ho, *et al.*, *J. Phys. Chem. Ref. Data* **1**, 279 (1972).
- [43] G. Abdullaev, *et al.*, *Phys. Status Solidi B* **13**, 315 (1966).
- [44] Q. Zheng, *et al.*, *Adv. Eng. Mater.* **21**, 1801342 (2019).
- [45] V. Konstantinov, *et al.*, *Low Temp. Phys.* **37**, 420 (2011).
- [46] K. Kim and M. Kaviany, *Phys. Rev. B* **94**, 155203 (2016).
- [47] R. Zheng, *et al.*, *Nat. Commun.* **2**, 289 (2011).
- [48] L. Crespi, *et al.*, *IEEE Electron Device Lett.* **35**, 747 (2014).
- [49] L. Tsetseris, *et al.*, *Phys. Rev. B* **89**, 035411 (2014).
- [50] P. E. Blöchl, *Phys. Rev. B* **50**, 17953 (1994).

- [51] G. Kresse and D. Joubert, *Phys. Rev. B* **59**, 1758 (1999).
- [52] J. P. Perdew, *et al.*, *Phys. Rev. Lett.* **77**, 3865 (1996).
- [53] G. Kresse and J. Furthmüller, *Comput. Mater. Sci.* **6**, 15 (1996).
- [54] G. Kresse and J. Furthmüller, *Phys. Rev. B* **54**, 11169 (1996).
- [55] H. J. Monkhorst and J. D. Pack, *Phys. Rev. B* **13**, 5188 (1976).
- [56] C. Coulais, *et al.*, *Nature* **561**, 512 (2018).
- [57] J. Crossno, *et al.*, *Science* **351**, 1058 (2016).
- [58] J. Bardeen and W. Shockley, *Phys. Rev. B* **80**, 72 (1950).
- [59] J. Xi, *et al.*, *Nanoscale* **4**, 4348 (2012).
- [60] Y. Cai, *et al.*, *J. Am. Chem. Soc.* **136**, 6269 (2014).
- [61] J.-H. Yang, *et al.*, *Nano Lett.* **16**, 1110 (2016).
- [62] Z. Zhu, *et al.*, *Phys. Rev. Lett.* **119**, 106101 (2017).
- [63] S. Plimpton, *J. Comput. Phys.* **117**, 1 (1995).
- [64] A. Kinaci, *et al.*, *Phys. Rev. B* **86**, 115410 (2012).
- [65] X. Xu, *et al.*, *Nat. Commun.* **5**, 3689 (2014).
- [66] H. Wang, *et al.*, *Nat. Commun.* **8**, 15843 (2017).
- [67] S. Lepri, *et al.*, *Phys. Rev. Lett.* **78**, 1896 (1997).
- [68] Z. Gao, *et al.*, *Phys. Rev. E* **93**, 022102 (2016).
- [69] C. N. Berglund and H. J. Guggenheim, *Phys. Rev.* **185**, 1022 (1969).
- [70] G. G. Naumis, *et al.*, *Rep. Prog. Phys.* **80**, 096501 (2017).
- [71] M. Ghorbani-Asl, *et al.*, *Phys. Rev. B* **87**, 235434 (2013).
- [72] C.-H. Chang, *et al.*, *Phys. Rev. B* **88**, 195420 (2013).
- [73] E. Scalise, *et al.*, *Nano Res.* **5**, 43 (2012).
- [74] M. Brandbyge, *et al.*, *Phys. Rev. B* **65**, 165401 (2002).
- [75] S. Smidstrup, *et al.*, *J. Phys.: Condens. Matter* **32**, 015901 (2019).
- [76] S. Datta, *Phys. Today* **49**, 70 (1996).
- [77] G. Liu, *et al.*, *Phys. Rev. B* **99**, 195436 (2019).
- [78] D. Yoon, *et al.*, *Nano Lett.* **11**, 3227 (2011).
- [79] D. Liu, *et al.*, *Phys. Rev. B* **94**, 165432 (2016).
- [80] T. Kambe, *et al.*, *J. Am. Chem. Soc.* **135**, 2462 (2013).
- [81] R. Sakamoto, *et al.*, *Chem. Commun.* **53**, 5781 (2017).
- [82] M. Treier, *et al.*, *Nat. Chem.* **3**, 61 (2011).
- [83] C. Moreno, *et al.*, *Science* **360**, 199 (2018).
- [84] H. Sugimoto, *et al.*, *RSC Adv.* **5**, 8427 (2015).
- [85] S. Liu, *et al.*, *Chem. Mater.* **30**, 6222 (2018).
- [86] M. Bieri, *et al.*, *Chem. Commun.* **45**, 6919 (2009).
- [87] L. F. Villalobos, *et al.*, *Sci. Adv.* **6**, eaay9851 (2020).
- [88] Q. Tan, *et al.*, *Chem. Commun.* **52**, 537 (2016).
- [89] W. Wang, *et al.*, *Nat. Commun.* **6**, 7853 (2015).
- [90] J. C. Meyer, *et al.*, *Nature* **446**, 60 (2007).